Valley Isospin Controlled Fractional Quantum Hall States in Bilayer Graphene

Ke Huang[1,2] Hailong Fu,[1] Danielle Reifsnyder Hickey[3,4] Nasim Alem,[4] Xi Lin,[2,5,6]
Kenji Watanabe[7] Takashi Taniguchi,[8] and Jun Zhu[1,9,*]

[1]*Department of Physics, The Pennsylvania State University, University Park, Pennsylvania 16802, USA*
[2]*International Center for Quantum Materials, Peking University, Beijing 100871, China*
[3]*Department of Chemistry, The Pennsylvania State University, University Park, Pennsylvania 16802, USA*
[4]*Department of Materials Science and Engineering, The Pennsylvania State University,*
University Park, Pennsylvania 16802, USA
[5]*Beijing Academy of Quantum Information Sciences, Beijing 100193, China*
[6]*CAS Center for Excellence in Topological Quantum Computation,*
University of Chinese Academy of Sciences, Beijing 100190, China
[7]*Research Center for Functional Materials, National Institute for Materials Science,*
1-1 Namiki, Tsukuba 305-0044, Japan
[8]*International Center for Materials Nanoarchitectonics, National Institute for Materials Science,*
1-1 Namiki, Tsukuba 305-0044, Japan
[9]*Center for 2-Dimensional and Layered Materials, The Pennsylvania State University,*
University Park, Pennsylvania 16802, USA

A two-dimensional electron system placed in a magnetic field develops Landau levels, where strong Coulomb interactions lead to the appearance of many-body correlated ground states. Quantum numbers similar to the electron spin enable the understanding and control of complex ground state order and collective excitations. Owing to its spin, valley, and orbital degrees of freedom, Bernal-stacked bilayer graphene offers a rich platform to pursue correlated phenomena in two dimensions. In this work, we fabricate dual-gated Bernal-stacked bilayer graphene devices and demonstrate unprecedented fine control over its valley isospin degrees of freedom using a perpendicular electric field. Higher sample quality enables us to probe regimes obscured by disorder in previous studies. We present evidence for a new even-denominator fractional quantum Hall state at filling factor $\nu = 5/2$. The $5/2$ state is found to be spontaneously valley polarized in the limit of vanishing valley Zeeman splitting, consistent with a theoretical prediction made regarding the spin polarization of the Moore-Read state. In the vicinity of the even-denominator fractional quantum Hall states, we observe the appearance of the predicted Levin-Halperin daughter states of the Moore-Read Pfaffian wave function at $\nu = 3/2$ and $7/2$ and of the anti-Pfaffian at $\nu = 5/2$ and $-1/2$. These observations suggest the breaking of particle-hole symmetry in bilayer graphene. We construct a comprehensive valley polarization phase diagram for the Jain sequence fractional states surrounding filling factor $3/2$. These results are well explained by a two-component composite fermion model, further demonstrating the SU(2) nature of the valley isospin in bilayer graphene. Our experiment paves the path for future efforts of manipulating the valley isospin in bilayer graphene to engineer exotic topological orders and quantum information processes.

Subject Areas: Condensed Matter Physics, Graphene

I. INTRODUCTION

Electrons occupying a partially filled Landau level (LL) experience strong Coulomb interactions that lead to a

*Corresponding author.
jzhu@phys.psu.edu

plethora of correlated electronic states, generally known as the fractional quantum Hall (FQH) effect. The FQH effect hosts complex many-body wave functions, nontrivial topology, and unconventional quantum exchange statistics that are potentially useful for topological quantum computing [1–9]. In particular, even-denominator states occurring at half fillings, such as the $\nu = 5/2$ state in GaAs [1,2,6], have attracted ongoing attention since the $5/2$ state is postulated to be a $p + ip$ superconductor and harbors non-Abelian excitations potentially useful in the construction of a topological qubit [3,5,10]. Its fundamental novelty and technological appeal have motivated many studies and the

discoveries of even-denominator FQH states with potentially similar origins in other 2D systems such as bilayer graphene [11–13], ZnO [14], and WSe_2 [15]. While thermal conductance measurements have provided good evidence on the non-Abelian nature of the 5/2 state [16], its exchange statistics has not been explicitly verified in interferometry studies. The particle-hole symmetry of the even-denominator states is fundamental to its understanding, as ground states of different symmetries belong to different topological orders and harbor different edge modes [2,17–22]. Furthermore, the Moore-Read wave function of the 5/2 state must be a spin triplet and is in fact expected to be spontaneously spin polarized in the limit of zero Zeeman splitting [3,10,23,24]. Experimental studies of these important issues remain ongoing [6].

The electron spin and spinlike degrees of freedom in new materials and artificial structures play a fundamental role in the formation of correlated phenomena through exchange interactions and the symmetry requirement of a many-body wave function [25–28]. Owing to its spin, orbital, and valley isospin degrees of freedom, the $E = 0$ octet of bilayer graphene (BLG) supports a rich variety of spontaneously broken symmetries and correlations [11,12,29–31]. In particular, a perpendicular electric displacement field D generated through dual gating controls the electrical valley Zeeman splitting E_v between states occupying different valleys or layers, thus offering a powerful experimental knob to control the character of the LLs and the nature of the interactions they support. This tuning is compatible with device scaling and is independent of the magnetic field B, which controls the strength of the Coulomb interactions. It is a distinct experimental control of the BLG platform, which can be deployed to construct

and elucidate many-body phenomena in a correlated, multicomponent 2D system.

In this work, we make ultra-high-quality BLG devices that enable fine control of the valley Zeeman splitting E_v, and we explore its profound impact in realizing FQH states with different ground state orders and valley isospin (VIS) polarizations. In the regime of low D field, an unprecedented even-denominator FQH state emerges at filling factor 5/2 and is found to be spontaneously valley polarized in the limit of vanishing E_v. We observe clear Levin-Halperin daughter states of either the Moore-Read Pfaffian or the anti-Pfaffian in the vicinity of $\nu = 7/2$, 3/2 (Pfaffian) and $\nu = 5/2$, $-1/2$ (anti-Pfaffian), with the appearance of a Hall resistance plateau at $\nu = 1 + 7/13$. These results suggest that the even-denominator FQH states in BLG break particle-hole symmetry, and the broken symmetry sensitively depends on the underlying interactions. We construct a comprehensive experimental phase diagram of the VIS polarization for odd-denominator FQH states in the range $0 < \nu < 2$. These measurements truly establish the valley isospin in BLG as a spinlike electronic degree of freedom and pave the pathway to future efforts exploiting its utility in controlling the ground state order and topology of correlated electronic states.

II. DEVICE FABRICATION

Our dual-graphite-gated, h-BN encapsulated Hall bar devices are made using dry van der Waals transfer and side contact techniques largely following methods introduced in the literature [11,12,32]. A different etching protocol is used in our fabrication process, which led to higher-quality electrical contacts compared to prior studies [11]. The details
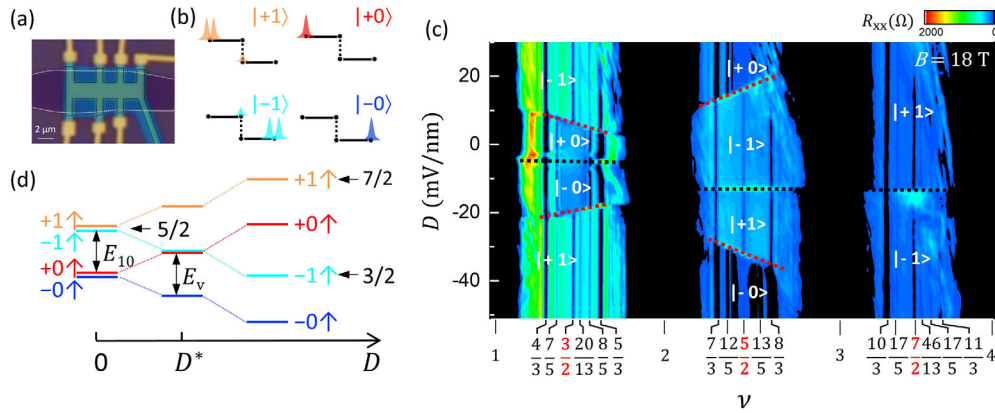

FIG. 1. Valley isospin controlled fractional quantum Hall states in bilayer graphene. (a) Optical micrograph of device 002. The BLG and the top graphite gate are etched into a Hall bar shape outlined in black. The bottom graphite gate is outlined in white. The thickness of the top and bottom BN sheets is 28 nm and 23 nm, respectively. See Appendix A for fabrication details. (b) Wave functions of LLs $|\xi, N\rangle$. Here, $\xi = +, -$ and $N = 0, 1$ denote the valley and orbital indices. (c) False color map of $R_{xx}(D, \nu)$ at $B = 18$ T and $T = 20$ mK. We label the parent LL of each region. D^* transitions are marked by red dashed lines. The black dashed lines mark the true $D = 0$ locations. States occupying the $|\pm 0\rangle$ LLs exhibit the two-flux CF Jain sequence shown in Fig. 10 in Appendix B. (d) Energy-level diagram that captures the qualitative features of panel (c). Even-denominator states at $\nu = 3/2$ and 7/2 are reported in Refs. [11,12].

of the fabrication are given in Appendix A. Figure 1(a) shows an optical micrograph of device 002. The carrier density n and displacement field D are, respectively, given by $n = g_{BG}(V_{BG} - V_{BG0}) + g_{TG}(V_{TG} - V_{TG0})$ and $D = [g_{BG}(V_{BG} - V_{BG0}) - g_{TG}(V_{TG} - V_{TG0})]e/2\varepsilon_0$, with the gating efficiencies $g_{BG} = 7.3 \times 10^{11}$ V^{-1} cm^{-2} and $g_{TG} = 5.9 \times 10^{11}$ V^{-1} cm^{-2} in device 002. Measurements used to characterize the devices, as well as parameters of devices 011 and 015, are also given in Appendix A.

III. RESULTS AND DISCUSSION

A. Even-denominator fractional quantum Hall state at $\nu = 5/2$

Figure 1(c) shows a false color map of the longitudinal resistance $R_{xx}(D, \nu)$ in the filling factor range $1 < \nu < 4$ at $B = 18$ T. Integer and fractional quantum Hall states appear as dark lines. They occupy the $|\pm 0\rangle$ and $|\pm 1\rangle$ LLs of the BLG, the wave functions of which are illustrated in Fig. 1(b) [29]. Figure 1(d) gives an energy level diagram of this regime. The valley Zeeman energy $E_v^\pm$ is defined as $E_v^\pm = \pm 1/2\ g_v D$, where $\pm 1/2$ corresponds to the quantum numbers of the two valley isospins and g_v is the bare valley g-factor. The valley Zeeman splitting E_v increases with increasing D following $E_v = g_v D$, with $g_v = 1.43$ K/(mV/nm). We obtain the value of g_v from Fig. 8 in Appendix B and Ref [30]. The $|+0\rangle$ and $|-1\rangle$ levels become degenerate at $D = D^*$, where $E_v = E_{10}$ [11,12,29,30]. This level crossing leads to the closing of gaps for states occupying these two LLs, resulting in an R_{xx} increase in our measurements. We mark the D^* transitions in Fig. 1(c) using four red dashed lines. In regimes of $D > D^*$, we observe the same LL orbitals as in previous studies, where two even-denominator FQH states at $\nu = 3/2$ and $7/2$ have been identified [11,12]. They also occur in our devices [see Fig. 1(c)]. In this work, we focus on the regime of $D < D^*$, where disorder has obscured previous studies [11,12].

In this small-D regime, states in the range of $2 < \nu < 4$ occupy the $|\pm 1\rangle$ LL levels. Remarkably, a strong R_{xx} minimum develops at $\nu = 5/2$ in our devices. This R_{xx} minimum occurs in multiple devices and is accompanied by a well-quantized R_{xy} plateau as shown in Fig. 9(a) of Appendix B. Thus, the state at $\nu = 5/2$ is an even-denominator FQH state. Its appearance on the $|\pm 1\rangle$ LL levels, while somewhat intuitive, is only observed now thanks to the high quality of our devices. As the LL diagram in Fig. 1(d) shows, the $5/2$ state resembles its counterpart in GaAs but with the spin index now replaced by the VIS index in BLG. A Moore-Read wave function requires the $5/2$ state to be polarized in any spin and isospin sectors while numerical simulations of a zero-thickness 2D system further support its spontaneous polarization in the limit of $E_z = 0$ [10,23,24]. Numerous experiments

have examined the spin polarization of the $5/2$ state in GaAs [6,33–40]. While the state is generally thought to be spin polarized in a sufficiently large magnetic field, measurements conducted in the low-field range of $B \leq 1$ T have uncovered potential phase transitions [36,37]. In the small-E_z regime, the interpretation of measurements is complicated by the finite wave-function thickness in GaAs and the changes of the interaction energies when the magnetic field changes. In comparison, the electrical tuning of E_v, together with the high quality and near-zero thickness of BLG, presents a clean approach to probe the valley isospin polarization in BLG, in advance of theoretical calculations.

We measure the gap of the $5/2$ state $\Delta_{5/2}$ as a function of the D field using thermally activated transport. Figure 2(a) plots the D-field sweeps of $R_{xx}^{5/2}(\tilde{D})$ measured at different temperatures, from which we obtain data points for $R_{xx}(T)$ and plot them in an Arrhenius plot in Fig. 2(b). Fits to $R_{xx}(T) \sim \exp(-\Delta/2k_B T)$ yield the gaps $\Delta_{5/2}(\tilde{D})$ at different D fields. Figure 2(c) plots $\Delta_{5/2}(\tilde{D})$ for both positive and negative values in the range of $|\tilde{D}| > 1$–2 mV/nm, where the effect of potential disorder can be neglected. Here, $\tilde{D} = D + 12.5$ mV/nm adjusts for a small offset in the applied D field. The bottom x axis of Fig. 2(c) plots the normalized E_v/E_c, where $E_c = (e^2/4\pi\epsilon\epsilon_0 l_B) = 217\sqrt{B[\text{T}]}$ K is the Coulomb energy scale in BLG using $\epsilon = 3$ for the dielectric constant of h-BN. The gap $\Delta_{5/2}(\tilde{D})$ saturates at 0.3 and 0.35 K, respectively, at large positive and negative D fields and extrapolates to a finite value of approximately 0.2 K at $\tilde{D} = 0$ from both sides. The trend $\Delta_{5/2}(\tilde{D})$ exhibits, together with a sizable gap at $E_v = 0$, provides strong experimental evidence for a spontaneously valley-polarized $5/2$ state. As we demonstrate in Fig. 4, the valley isospin in BLG indeed behaves as an SU(2) spin. The spontaneous valley polarization of the $5/2$ state is consistent with numerical simulations performed for the real electron spin of the Moore-Read state [23,24]. Prior work in BLG finds that the even-denominator state at $\nu = 3/2$ is spin polarized at 17 T [11]. Given the similar Zeeman splitting in both cases, we expect the $5/2$ state examined here to also be spin polarized, thus satisfying the triplet requirement of the Moore-Read wave function in any spin or isospin [3].

Figure 2(d) shows the behavior of $R_{xx}^{5/2}(\tilde{D})$ and $\Delta_{5/2}(\tilde{D})$ close to $\tilde{D} = 0$, where the valley polarization of the $5/2$ state is expected to switch abruptly in samples free of disorder. Instead, we observe a percolation transition from the $|+1\rangle$ LL to the $|-1\rangle$ LL with a full width of approximately $\delta D \sim 0.7$ mV/nm or $\delta E_v \sim 1$ K. This transition is signaled by two approximately T-independent crossover points at $D_c \sim \pm 0.35$ mV/nm in Fig. 2(d), where $\Delta_{5/2}$ apparently drops to zero. We emphasize that the T dependence of R_{xx} close to $\tilde{D} = 0$ is not related to the
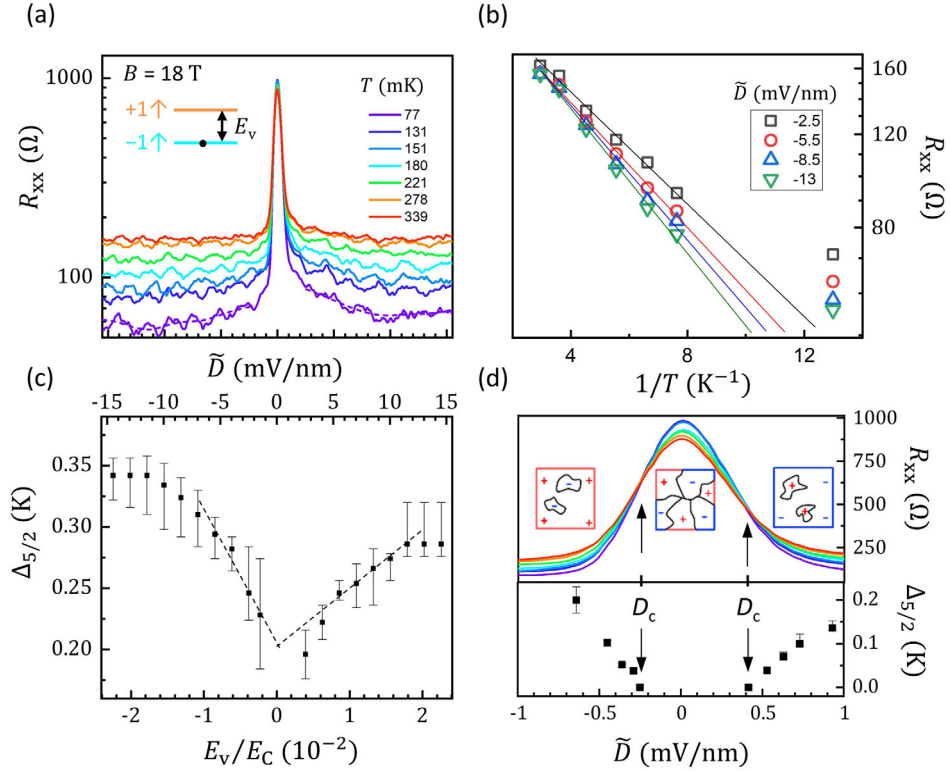
FIG. 2.   The gap of the 5/2 state. (a) $R_{xx}^{5/2}(\tilde{D})$ sweeps at selected temperatures as labeled in the plot. Here, both gates are swept simultaneously to stay on the $\nu = 5/2$ minimum. Data points are read from smoothed traces, an example of which is shown for the 77-mK trace (violet dashed line). (b) T-dependent R_{xx} obtained from traces in panel (a) and plotted on an Arrhenius plot for selected D fields as labeled. Solid lines are fits to $\exp(-\Delta_{5/2}/2k_B T)$, from which we extract $\Delta_{5/2}$. Upper and lower bounds of $\Delta_{5/2}$ from the fits are shown as error bars in panel (c). Here, we obtain $\tilde{D} = D + 12.5$ mV/nm using the black dashed line crossing $\nu = 5/2$ in Fig. 1(c). (c) $\tilde{D}$ dependence of $\Delta_{5/2}$. Dashed lines extrapolate to 0.2 K at $\tilde{D} = 0$. Note that $\Delta_{5/2}$ is larger on the negative D side due to weaker screening from the top graphite gate, which is farther away. (d) Upper panel: T dependence of R_{xx} at very small $\tilde{D}$. As the insets illustrate, the sample is comprised of domains of opposite valley polarizations near $\tilde{D} = 0$, and the dominance of bulk conduction leads to $R_{xx} \sim 1/\sigma_{xx}$ and a negative dR/dT. The transition to edge conduction at large $\tilde{D}$ produces roughly T-independent crossover points at $D_c \sim \pm 0.3$ mV/nm labeled by the arrows. The lower panel of (d) plots the extracted $\Delta_{5/2}$. Note that $\Delta_{5/2}$ drops precipitously towards zero at D_c. Similar percolation transitions accompany other valley polarization transitions that occur at both integer and fractional fillings in our samples, such as shown in Figs. 4 and 12.

physics of the 5/2 state but rather reflects the general conduction behavior of a percolation network; the increased bulk conduction in the presence of mixed valley domains leads to $R_{xx} \sim \sigma_{xx}^{-1}$, hence, an opposite dR/dT near $\tilde{D} = 0$. The low disorder of our devices allows us to probe the intrinsic behavior of the 5/2 state down to the small valley Zeeman splitting of $E_v/E_c \sim 10^{-3}$, where the 5/2 state remains valley polarized.

B. Particle-hole symmetry of the even-denominator fractional quantum Hall states

The particle-hole (p-h) symmetry of a half-filled LL is another open question of keen interest to the quantum Hall community [2,16–22,41–45]. The Moore-Read Pfaffian and its p-h conjugate, the anti-Pfaffian, explicitly break the p-h symmetry. Their energy difference is small, and

each state has gained support in numerical calculations performed in GaAs [17,18,41–43]. Theory also suggests the possibility of a third ground state, known as the p-h Pfaffian, which preserves the p-h symmetry and can be stabilized when both disorder and LL mixing are included [44,45]. The different Majorana neutral modes of the three distinct topological orders allow them to be differentiated in thermal conductance and noise measurements, and recent experimental results have favored the p-h Pfaffian [16,22]. However, the situation is far from being settled. In the hierarchical theory, quasiparticles and quasiholes away from the half-filled $N = 1$ LL condense into incompressible fractional quantum Hall states known as the Levin-Halperin states [46]. The first daughter states of the Pfaffian occur at partial fillings $\tilde{\nu} = 7/13$ and $8/17$, while the first daughter states of the anti-Pfaffian occur at $\tilde{\nu} = 6/13$ and $9/17$ [46]. Transport studies in GaAs have revealed the
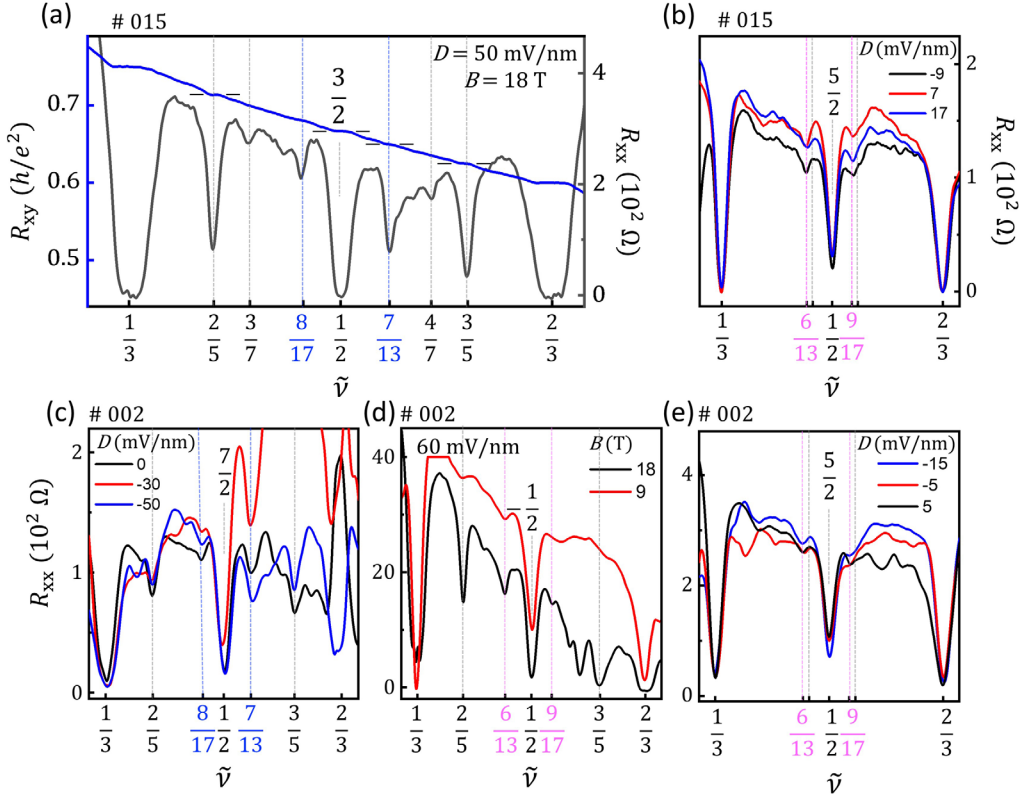
FIG. 3. Particle-hole asymmetry at half-filled $N = 1$ LLs in BLG. Panels (a)–(e) plot R_{xx} as a function of the partial filling $\tilde{\nu} = \nu - [\nu]$ near $\nu = 3/2$ (a), $5/2$ (b), $7/2$ (c), $-1/2$ (d), and $5/2$ (e), respectively. Panel (a) also plots R_{xy} measured concomitantly. Panels (a) and (b) are from device 015, and (c)–(e) are from device 002. The data are obtained at fixed D fields as labeled, and $B = 18$ T unless otherwise noted. Here, $T = 20$ mK. In panel (a), R_{xy} plateaus are observed at $\tilde{\nu} = 2/5$, $1/2$, $7/13$, and $3/5$ and quantized to the correct values given by their full filling factors. Weak but reproducible R_{xx} minima occur at $\tilde{\nu} = 8/17$, $3/7$, and $4/7$. In panels (a)—(e), dashed lines mark fractional fillings calculated from the positions of $1/3$ and $2/3$. Only reproducible minima are marked. Blue lines mark $\tilde{\nu} = 8/17$ and $7/13$, and magenta lines mark $\tilde{\nu} = 6/13$ and $9/17$. Their differences, though small, are discernable in our data. Additional data on $\nu = 3/2$ and $-5/2$ from device 002 are given in Fig. 11 of Appendix B.

appearance of a clear FQH state at $\tilde{\nu} = 6/13$, suggesting an anti-Pfaffian ground state [21]. The understanding and reconciling of these measurements remain ongoing. BLG exhibits multiple even-denominator FQH states including the new $5/2$ state. Using the Levin-Halperin states as indicators, our transport studies point to the Pfaffian order at $\nu = 3/2$, $7/2$ and the anti-Pfaffian order at $\nu = 5/2$, $-1/2$.

The p-h asymmetry appears to be most prominent at $\nu = 3/2$, as shown in Fig. 3(a) for device 015 and Fig. 11(a) for device 002. We see clear R_{xx} minima at $\tilde{\nu} = 7/13$ and $8/17$, together with a Hall plateau at $R_{xy} = 0.65 \, h/e^2$ corresponding to the $20/13$ filling. Strong R_{xx} minima at these fractional fillings are also found in device 002 and shown in Fig. 11(a). In the literature, a peak at $7/13$ was also found in the capacitance measurements of Ref. [12]. In contrast, the newly observed $5/2$ state appears to follow the anti-Pfaffian order, as suggested by the appearance of R_{xx} minima at $\tilde{\nu} = 6/13$ and $9/17$, as labeled in Fig. 3(b). Figures 3(b) and 3(e) show their appearance in both devices

015 and 002. The R_{xx} minima, though shallow, appear at the same fractions over a wide range of the D field and are robust in thermal cycling. It is useful to compare their weak but robust appearance with other accidental and irreproducible minima in R_{xx}, a number of which can be seen in Figs. 3(c)–3(e). Following the same reproducibility criteria, we identify the $\nu = 7/2$ state to be Pfaffian [Fig. 3(c)] and the $\nu = -1/2$ state to be anti-Pfaffian [Fig. 3(d)]. In the vicinity of all four even-denominator states, we find the daughter states of either the Pfaffian or the anti-Pfaffian, but not both, and the daughter states always appear in tandem on both sides of the half-filling. In addition, we see a weak but robust appearance of the $\tilde{\nu} = 6/13$ state near $\nu = -5/2$ [Fig. 11(b)], suggesting that the $-5/2$ state is likely anti-Pfaffian also. Table I summarizes the broken p-h symmetries of five even-denominator states in BLG. Subtle differences of the interaction at different filling factors play a clear role in the resulting asymmetry, and calculations capable of explaining all of them self-consistently will shed

TABLE I.　Ground state wave function symmetry of the even-denominator states in BLG.

ν	3/2	5/2	7/2	$-1/2$	$-5/2$
P-H symmetry	Pf	aPf	Pf	aPf	aPf*(likely)

much theoretical light on this fundamental question. Finally, we briefly note the appearance of unconventional FQH states at $\tilde{\nu} = 2/5, 3/5, 3/7$, and $4/7$ in Fig. 3(a), especially the well-developed 2/5 and 3/5 states exhibiting quantized R_{xy} plateaus. These observations offer the future possibility of exploring the proposed non-Abelian orders and topological phase transitions in BLG [4,47].

C. Valley isospin polarization transitions of odd-denominator fractional quantum Hall states

The understanding and control of the spin or isospin configuration of a FQH state is a fundamental and key step

towards the generation of parafermions [2,7,26,48,49]. The ease of tuning E_v and ν continuously in a single device enables us to systematically study the ground state VIS polarization of FQH states. Figures 4(a) and 4(b) show maps of $R_{xx}(D, \nu)$ near $D = 0$ for $4/3 < \nu < 5/3$ and $1/3 < \nu < 2/3$, respectively. In Fig. 4(a), we observe numerous gap closing points reminiscent of spin or pseudospin transitions observed in other 2D systems [2,26,48,49]. Similar gap closing points, also in the vicinity of D^*, were observed in Ref. 12 and interpreted using an effective single-particle-like model [12]. Here, we examine our data in the theoretical framework of two-flux composite fermions (CFs) with SU(2) spins or isospins. In this model, the fractional filling ν near $3/2$ maps to ν^* filled CF Λ levels through $\nu = 2 - \nu^*/(2\nu^* \pm 1)$. As illustrated in Fig. 4(c), VIS (partial) polarization transitions occur when Λ levels of opposite valley indices cross one another. This condition corresponds to $E_v = [1 - \nu^*, 3 - \nu^*, \ldots, \nu^* - 1]\hbar\omega_c^*$, for a total number of ν^* transitions for the ν^*th Λ level. Here, $\omega_c^* = (eB_{\text{eff}}/m_{3/2}^*)$ is the cyclotron frequency of CFs, $B_{\text{eff}} = 3(B - B_{3/2})$, and $m_{3/2}^*$ is the effective polarization
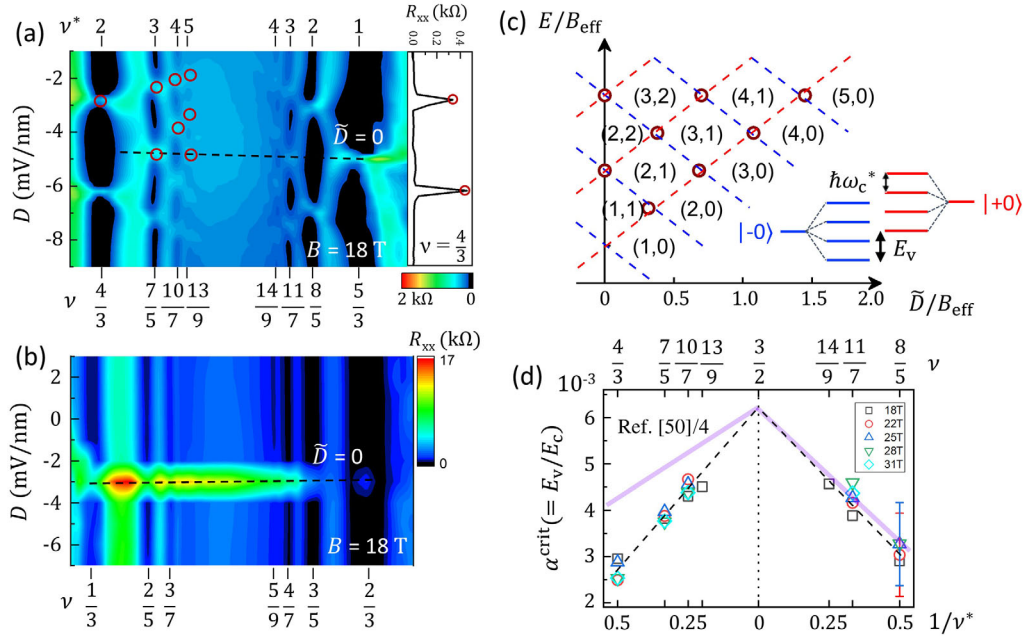

FIG. 4.　Valley isospin polarization of Jain FQH states. (a,b) False color maps of $R_{xx}(D, \nu)$ similar to Fig. 1(c) in the filling factor ranges of $4/3 < \nu < 5/3$ (a) and $1/3 < \nu < 2/3$ (b). The map in panel (a) expands upon the low-D region between the red dashed lines in Fig. 1(c). The top axis in panel (a) labels the corresponding CF Λ level filling factor ν^*. The side panel of panel (a) plots a line cut through $\nu = 4/3$. The red circles mark $\tilde{D} \geq 0$ VIS transitions for $\nu = 4/3, 7/5, 10/7$, and $13/9$. Data taken at $B = 18$ T and $T = 20$ mK. No transitions are observed in $1/3 < \nu < 2/3$. (c) Free CF Λ level fan diagram including valley isospin. The blue and red dashed lines represent Λ levels of the "+" and "−" valley polarizations, respectively, and (n_-, n_+) labels the filling factor of each valley. Here, $\nu^* = n_- + n_+$. The slope of the red dashed lines is obtained through a fit to $E_v = (\nu^* - 1)\hbar\omega_c^*$. This fit yields $m_{3/2}^* = 2.6m_e$, which determines the rest of the diagram. Open circles correspond to transitions marked by the same symbol in panel (a). A similar analysis is performed for states with $\nu > 3/2$ and yields a smaller $m_{3/2}^* = 1.9m_e$. See Fig. 13 in Appendix B for the fits in both regimes. (d) Normalized critical valley Zeeman energy α^{crit} for FQH states on both sides of $\nu = 3/2$ at fixed magnetic fields as labeled in the plot. The solid violet lines plot calculations from Ref. [50] divided by 4.

mass at $\nu = 3/2$ [2]. With a single fitting parameter $m_{3/2}^* = 2.6 m_e$, where m_e is the free electron mass in vacuum, we can capture all eight transitions marked by red circles in Fig. 4(a). In stark contrast to $4/3 < \nu < 5/3$, no valley polarization transitions are observed for states in $1/3 < \nu < 2/3$ in magnetic fields ranging from 14 T to 31 T, suggesting all two-flux CFs in the last LL are spontaneously valley polarized. Following a similar argument, we surmise that the even-denominator FQH states at $\nu = 7/2$ and $-1/2$ may also be spontaneously valley polarized [Fig. 1(c) and Refs. [11,12]], though measurements performed in Fig. 2 for $\nu = 5/2$ are required to confirm this hypothesis. The different behaviors of the FQH states in the two regimes connected by ν to $2 - \nu$ transformation point to a strong LL mixing effect [2].

Extending similar measurements and analysis to higher magnetic fields (18–31 T), we plot in Fig. 4(d) the normalized critical valley Zeeman energy $\alpha^{\text{crit}} = E_{\text{v}}/E_c$ corresponding to the onset of full valley polarization (see Fig. 12 in Appendix B for raw data). Here, $E_c = (e^2/4\pi\epsilon\epsilon_0 l_B) = 217\sqrt{B[\text{T}]}$ K is the Coulomb energy scale in BLG using $\epsilon = 3$ for the dielectric constant of h-BN. Results from different magnetic fields collapse quite well, suggesting an approximate $\sqrt{B}$ scaling of $m_{3/2}^*$. The tentlike solid lines in Fig. 4(d) represent exact diagonalization calculations performed for spin polarization transitions in a zero-thickness 2D system [50], which is applicable to any SU(2) isospins. The qualitative agreement between our data and theory supports the SU(2) character of the VIS in BLG. Quantitatively, our results of α^{crit} are more symmetric around $3/2$ and are approximately 4–5 times smaller than theory. Extrapolation to $3/2$ yields $m_{3/2}^* \sim 0.50 m_e \sqrt{B}$, in comparison to the theoretical value of $0.13 m_e \sqrt{B}$ in graphene [50]. Measurements on device 011 yield nearly identical transitions (Fig. 14), indicating that the underlying physics is insensitive to sample details. We attribute the small α^{crit} to the effect of LL mixing, the inclusion of which is necessary to accurately capture the energetics of correlated phenomena in BLG [51].

IV. CONCLUSION

In summary, we report the observation of an even-denominator FQH state at filling factor $5/2$ in Bernal-stacked bilayer graphene. The state remains polarized in the limit of vanishing valley isospin splitting, offering indirect support to a spontaneously spin-polarized Moore-Read state. The even-denominator states are particle-hole asymmetric, with the asymmetry consistent with a Pfaffian order at filling factors $3/2$ and $7/2$ and the anti-Pfaffian order at $5/2$ and $-1/2$. The valley isospin behaves like an SU(2) spin with excellent experimental maneuverability. We demonstrate the control of the ground state valley polarization of a large family of FQH states and envision the manipulation of valley isospin to be a powerful tool in elucidating other correlated electronic phenomena and constructing quantum information devices.

APPENDIX A: DEVICE FABRICATION AND CHARACTERIZATION

1. Device fabrication

We fabricated our devices using the processes described below. The top/bottom h-BN sheet thickness is 28 nm/23 nm, 24 nm/27 nm, 35 nm/35 nm, and 25 nm/25 nm, respectively, for devices 002, 011, 012, and 015. We performed transport measurements on devices 002, 011, and 015 and microscopy studies on device 012. Figure 5(a) shows a scanning electron microscopy (SEM) image of device 012. Figures 5(b) and 5(c) show cross-sectional scanning transmission electron microscopy (STEM) or TEM images of two slabs lifted from the
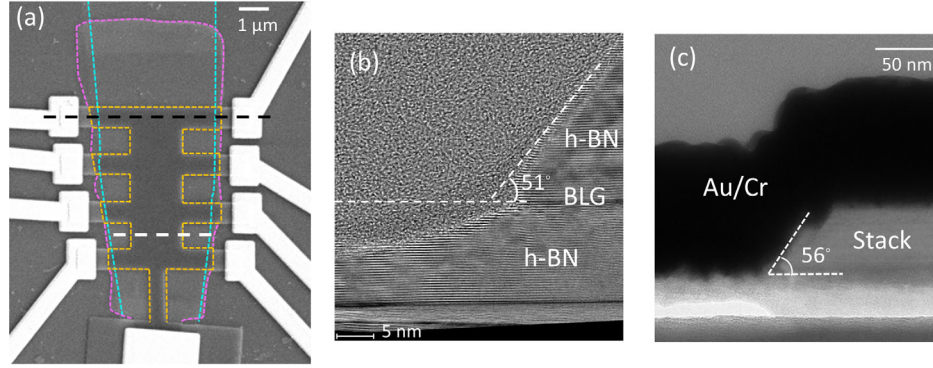
FIG. 5. Microscopy studies. (a) SEM image of device 012. The bottom graphite gate and the bottom h-BN sheet are outlined in cyan and magenta dashed lines, respectively. The orange dashed line outlines the Hall bar profile of the top h-BN/BLG stack. (b) High-resolution bright-field STEM image of the cross section cut through the white dashed line in panel (a). (c) Conventional TEM image of the cross section cut through the black dashed line in panel (a), showing the Au/Cr side contact. The etching profiles resemble those of previous studies.

two locations marked in Fig. 5(a) using a focused ion beam (FIB). The sample preparation and microscopy measurements follow that of Ref. [32]. TEM studies were performed using an FEI Titan³ G2 operating at 200 kV and an

FEI Talos F200X operating at 80 kV. SEM imaging and FIB TEM sample preparation were performed on a Thermo Scientific Scios 2 DualBeam analytical FIB-SEM using ion beam voltages ranging from 30 kV down to 5 kV for lamella thinning.

To make a device we first build a h-BN/graphene/h-BN/ bottom graphite gate stack and transfer it to SiO_2/Si substrate using a dry transfer method [28,30]. This process is followed by annealing in an Ar/O_2 atmosphere at 450 °C for 3 hours to remove polymer residue from the transfer. We then exfoliate a graphite sheet (3–4 nm thick) on a PPC (polypropylene carbonate) stamp and transfer it to the stack. This will be the top gate. Figure 6(a) shows a schematic of the finished stack.

A sequence of e-beam lithography and reactive ion etch (RIE) steps illustrated in Figs. 6(b)–6(f) is used to shape the stack into the Hall bar structure shown in Fig. 1(a). We first etch the top graphite sheet into an area that is slightly larger than the bottom graphite gate to expose the h-BN/BLG area reserved for making contacts later [Fig. 6(b)]. We then use e-beam lithography to define the Hall bar structure [Fig. 6(c)] and three sequential etching steps to pattern the top gate/h-BN/BLG stack. The three steps are illustrated in Figs. 6(d)–6(f). The CHF_3/O_2 etching step in Fig. 6(d) was done unintentionally for device 002 and repeated in devices 011, 012, and 015. In this step, the top graphite gate protects the h-BN/BLG underneath from being etched, and the etching time is not long enough to fully remove the top h-BN sheet in areas outside the top graphite sheet. Device 703 was made without this step, and we compare their performances in Fig. 7. We then use O_2 plasma to shape the top graphite gate [Fig. 6(e)] followed by a CHF_3/O_2 plasma to etch the h-BN/BLG stack into the Hall bar structure [Fig. 6(f)]. Table II shows the parameters used for the two types of plasma. Etching times for device 002 are shown in Fig. 6 and adjusted for other devices.
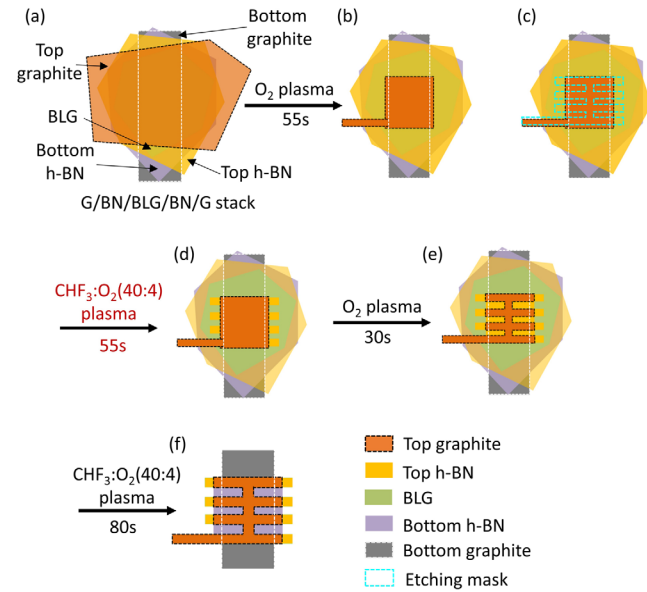

FIG. 6. The etching steps used in the fabrication of device 002. (a) Illustration of the finished graphite/h-BN/BLG/h-BN/graphite five-layer stack. (b) Illustration of the shape of the top graphite sheet after the O_2 etch. It extends over the bottom graphite gate (white dashed lines) by about 200 nm on the left and right sides. (c) Etching mask used in the next three etching steps on panel (b). (d) CHF_3/O_2 etch defining the shape of the terminals outside the top graphite sheet. The h-BN/BLG underneath the top graphite sheet remains intact. The entire BLG sheet is not exposed in this step. (e) O_2 etch, which defines the shape of the top graphite gate. (f) Finished Hall bar device.
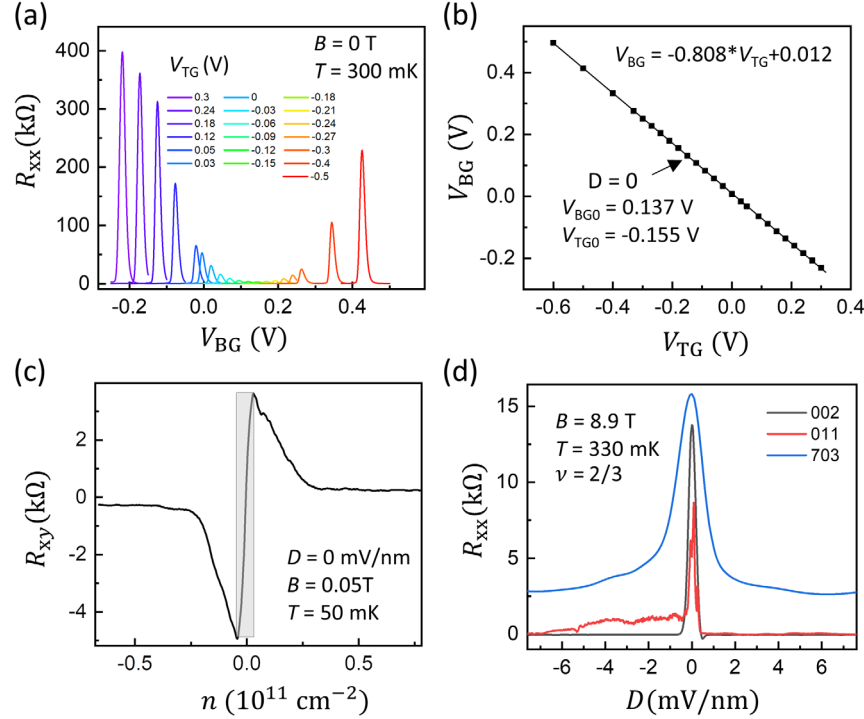
FIG. 7. Device characterization. (a) R_{xx} as a function of V_{BG} at fixed V_{TG}'s as indicated in the plot. Tracking the peaks allows us to determine the gating relation of V_{BG} and V_{TG}, which is plotted in panel (b). The global minimum occurs at $D = 0$, which corresponds to $V_{BG0} = 0.137$ V and $V_{TG0} = -0.155$ V. (c) Hall resistance $R_{xy}(n)$ at $B = 0.05$ T, $T = 50$ mK, and $D = 0$ mV/nm. The shaded region gives an estimated disorder-induced density broadening of $\delta n = 7 \times 10^9$ cm^{-2}. (a)–(c) Device 002. (d) $R_{xx}(D)$ sweeps obtained at the $\nu = 2/3$ minimum in three devices as labeled in the plot. The FWHM $\delta D = 0.38, 0.24$, and 1.43 mV/nm, respectively, for devices 002, 011, and 703. Traces are shifted horizontally to overlap the peaks at $D = 0$.

Finally, we pattern and deposit one-dimensional Au/Cr side contacts using e-beam lithography and physical vapor deposition. The substrate is cooled to 5 °C and rotated during the deposition. The deposition rate and thickness for each metal are as follows: Cr: 0.5 Å/s, 5 nm and Au: 1.5 Å/s, 45 nm.

2. Device characterization

Contacts in our devices reside outside the top and bottom graphite gates and are doped by the Si backgate. We apply $V_{Si} = 60$ V to ensure good performance in a large magnetic field. While STEM images in Figs. 5(b) and 5(c) do not reveal visible topographic differences compared to

previously reported devices [32], electrical contacts in our devices appear to perform better compared to R_{xx} traces shown in the literature, as indicated by less noisy, non-negative values when R_{xx} vanishes at integer and fractional fillings [11,52]. More robust contacts may have facilitated the observations of the even-denominator state at $\nu = 5/2$ and the valley polarization transitions of the fractional quantum Hall states, which are absent in previous transport studies [11,12]. A second distinguishing feature devices 002 and 011 exhibit is the very narrow valley polarization transition peak at $D = 0$, which is a strong indicator of higher sample quality. Figure 7(d) compares $R_{xx}(D)$ traces taken at the $\nu = 2/3$ minimum in devices 002, 011, and 703. Both 002 and 011 are fabricated with the CHF$_3$/O$_2$ etching step highlighted in red in Fig. 6 while 703 is fabricated without this step. The full width at half maximum of the $D = 0$ peak δD is, respectively, 0.38, 0.24, and 1.43 mV/nm in devices 002, 011, and 703. While it remains unclear to us how the extra etching step reduces δD, a small disorder broadening of the valley Zeeman splitting is crucial to the observations reported in this work.

We use the top and bottom graphite gates to tune the carrier density n and the perpendicular electric

TABLE II. Parameters used in the RIE processes.

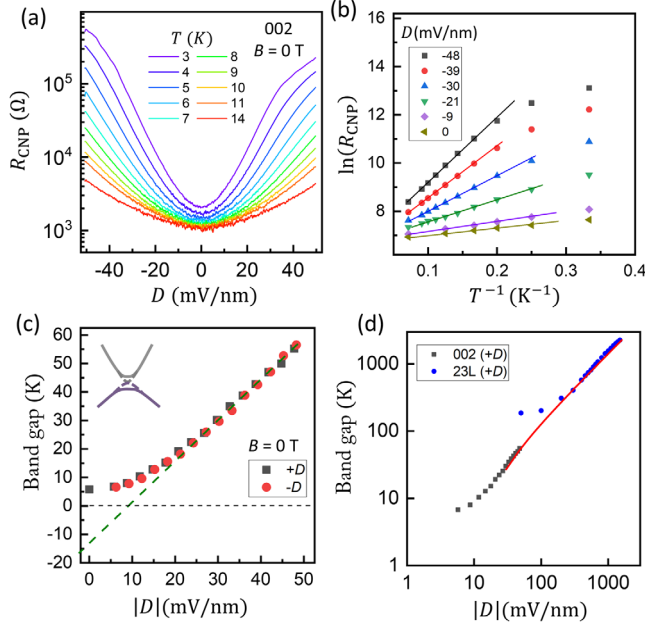| Gas	Pressure (mTorr)	Temperature (°C)	RF forward power (W)	Flow (sccm)
O$_2$	20	25	14	25
CHF$_3$ + O$_2$	75	25	40	CHF$_3$: 40 O$_2$: 4

FIG. 8. The D-field dependence of the band gap in BLG. (a) Charge neutrality point resistance R_{CNP} as a function of D at different temperatures. (b) T-dependent R_{CNP} obtained from traces in panel (a) and plotted on an Arrhenius plot for selected D fields as labeled. Solid lines are fits to $\exp(-\Delta/2k_BT)$, from which we extract Δ. (c) Extracted $\Delta(D)$ for both positive and negative D fields. We fit data above 20 mV/nm with a line corresponding to $\Delta(D) = 1.43D - 16$ [K] (green dashed line). Disorder leads to the reduction of Δ, which manifests as a negative offset of 16 K. The formation of electron-hole puddles at the CNP gives rise to a finite energy scale of 5 K at $D = 0$. Both point to bulk disorder on the scale of about 10 K, similar to other state-of-the-art BLG devices. (d) Data from device 002 here and 23L in Ref. [30]. The red line corresponds to the fit obtained in panel (c).

displacement field D following established practices [28,30]. Figure 7(a) plots the longitudinal resistance R_{xx} as a function of the bottom gate voltage V_{BG} at fixed top gate voltage V_{TG} in device 002. Tracking the charge neutrality points (CNP) (R_{xx} peaks) yields the gating relation $V_{BG} = -0.81 \times V_{TG} + 0.012$ as well as (V_{BG0}, V_{TG0}) corresponding to the $D = 0$ point marked in Fig. 7(b).

Figure 7(c) plots the Hall resistance R_{xy} vs n at $B = 0.05$ T in device 002, from which we estimate a disorder-induced density broadening of $\delta n = 7 \times 10^9$ cm^{-2}. Note that δn is typical of our dual-graphite-gated devices and comparable to what is reported in the literature [11,12]. In Fig. 8, we show that device 002 exhibits a *bulk* disorder energy scale of about 10 K, similar to other high-quality BLG devices reported in the literature [52]. However, transport in the quantum Hall regime is carried by edge states and as a result sensitively depends upon disorder close to the sample edges. Our devices that were fabricated using the process illustrated in Fig. 6 show unprecedented quality in this measurement, as indicated by the narrow peaks that devices 002 and 011 exhibit at the FQH state $\nu = 2/3$ in Fig. 7(d).

APPENDIX B: SUPPORTING MEASUREMENTS ON DEVICE 002

1. Measurement of the bare valley Zeeman g-factor g_v

We define the valley Zeeman energy $E_v^\pm = \pm 1/2 g_v D$, where $\pm$ corresponds to the two valley indices and g_v is the bare valley g-factor. The valley Zeeman splitting between the "+" and the "−" levels is $E_v = g_v D$. For the $N = 0$ orbital, $E_v = U$, where U is the potential difference between the top and bottom graphene layers.
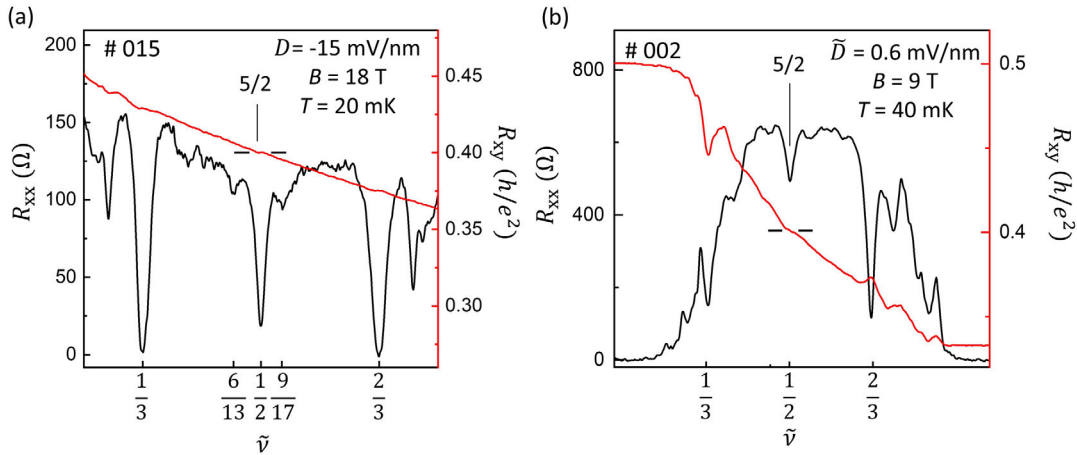

FIG. 9. The R_{xx} and R_{xy} vs filling factor ν near 5/2. (a) Deep R_{xx} minimum and a quantized R_{xy} plateau observed in device 015. (b) Signatures of the 5/2 state still present at $B = 9$ T and $T = 40$ mK in device 002.
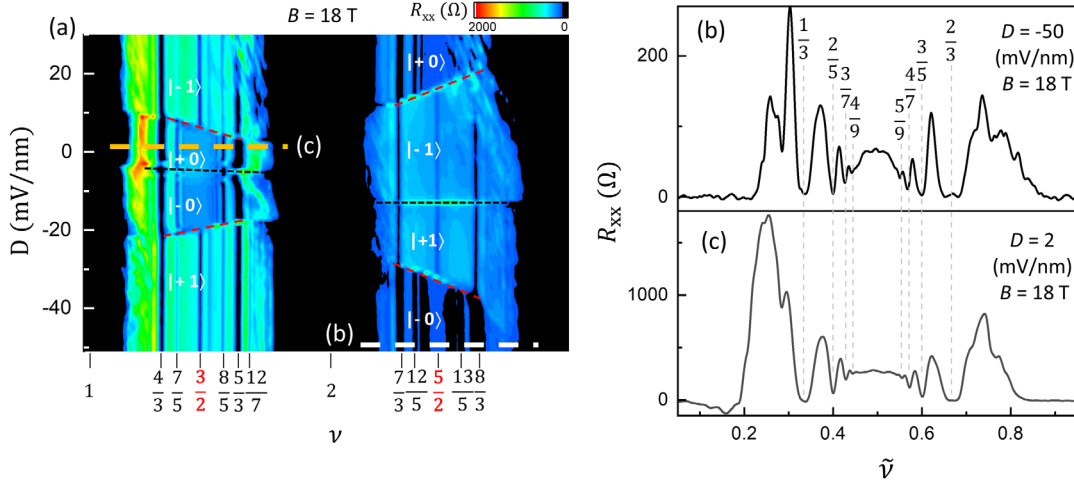
FIG. 10.   FQH states on the $N = 0$ LL. (a) Same false color map of R_{xx} (D, ν) as in Fig. 1(c) in the main text. (b) Trace of R_{xx} (ν) for $2 < \nu < 3$ following the white dashed line in panel (a). (c) Trace of R_{xx} (ν) for $1 < \nu < 2$ following the orange dashed line in panel (a). The two-flux composite fermion FQH states corresponding to $\tilde{\nu} = \nu - [\nu] = p/(2p \pm 1)$, where p is an integer, are labeled in panels (b) and (c) and provide an excellent description of the data. Here, $B = 18$ T, $T = 20$ mK.

Note that $U(D)$ increases linearly with the applied D field and equates the band gap in bilayer graphene $\Delta(D)$ at zero magnetic field when D is not too large [53]. We measure $\Delta(D)$ at $B = 0$ to determine the bare valley Zeeman g-factor g_v using $\Delta(D) = g_v D$. Figures 8(a)–8(c) show our measurements and analysis of $\Delta(D)$, following approaches described in the supplementary information of Ref. [30] and extending the data of Ref. [30] to the small-D regime. Our analyses yield $g_v = 1.43$ K/mV nm^{-1}, in excellent agreement with previous results [30].

2. FQH states occupying the $N = 0$ and 1 Landau levels

Figure 9 shows concomitant measurements of R_{xy} and R_{xx} near $\nu = 5/2$ in two devices. Device 015 exhibits a well-quantized plateau in R_{xy} at 18 T while device 002 exhibits a developing R_{xy} plateau down to 9 T, both confirming the $5/2$ state to be a FQH state. Figure 10 shows examples of FQH states occupying the $N = 0$ LL. They are well described by two-flux composite fermions. Figure 11 provides additional evidence to support the breaking of the particle-hole symmetry near even-denominator FQH states $\nu = 3/2$ and $-5/2$ in bilayer graphene. The Levin-Halperin states manifest as R_{xx} minima at the expected filling factors. They are robust in thermal cycling and appear reproducibly at the same filling factors in different D fields [Fig. 11(a)] and B fields

[Fig. 11(b)]. We are able to resolve the small differences between the two sets of filling factors, e.g., between $6/13$ and $8/17$, here and in the data shown in Fig. 3 of the main text.
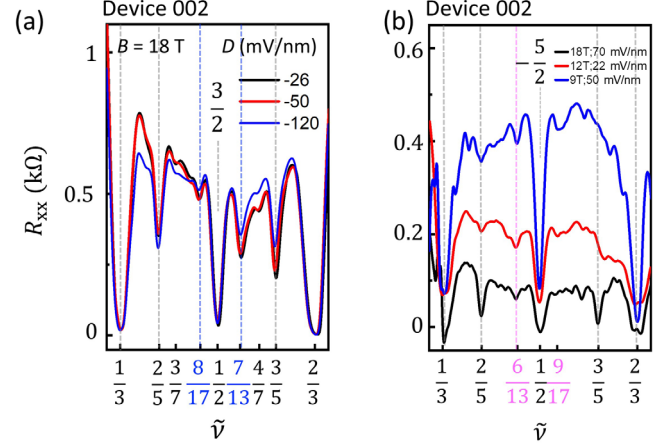

FIG. 11.   Additional data from device 002 showing the particle-hole asymmetry near the even-denominator FQH states in bilayer graphene. (a) R_{xx} (ν) at selected D fields in the vicinity of $\nu = 3/2$ showing the appearance of Levin-Halperin states at $\tilde{\nu} = 8/17$ and $7/13$. (b) R_{xx} (ν) at different B and D fields in the vicinity of $\nu = -5/2$. The appearance of the weak but reproducible $\tilde{\nu} = 6/13$ state suggests an anti-Pfaffian state, although the $\tilde{\nu} = 9/17$ is missing. Here, $T = 20$ mK.
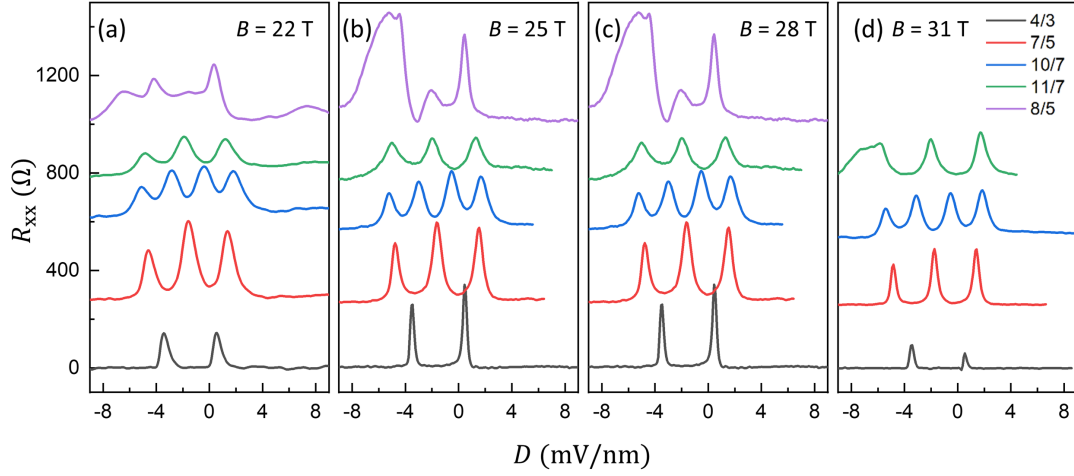
FIG. 12. Valley isospin polarization transitions of the FQH states near $\nu = 3/2$. (a)–(d) Traces taken at different B fields as labeled and at different fractions using the color scheme labeled in panel (d). Here, $T = 350$ mK. VIS transitions manifest as resistance peaks. The middle peaks of the red trace and the green trace mark the true $D = 0$ locations. We interpolate or extrapolate them linearly to find the $D = 0$ locations for the black and the blue traces. Data points in Fig. 4(d) correspond to readings of positive D's from device 002.

3. Valley isospin polarization transitions of the FQH states near $\nu = 3/2$

Figure 12 shows the measured $R_{xx}(D)$ traces from which we extract the data points plotted in Fig. 4(d) of the main text. In Fig. 13, we plot transitions to a fully VIS polarized ground state at $B = 18$ T for filling factors 4/3, 7/5, 10/7, and 13/9 (open red triangles) and 5/3, 8/5, 11/7, and 14/9 (open black squares). The data points are read from Fig. 4(a) of the main text and fit to the free CF model

$$E_v^{crit} = (\nu^* - 1)(\hbar e B_{eff}/m_{3/2}^*), \quad (B1)$$

from which we obtain effective polarization mass of $m_{3/2}^* = 2.6 m_e$ and $1.9 m_e$, respectively, using data from the regimes of $\nu < 3/2$ and $\nu > 3/2$.
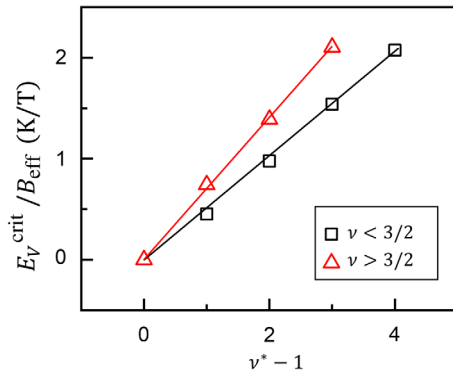

FIG. 13. Effective polarization mass of the CFs at $\nu = 3/2$. (a) E_v^{crit} vs $(\nu^* - 1)$ for $\nu = 4/3$, 7/5, 10/7, 13/9 ($\nu^* = 2, 3, 4, 5$, respectively, black symbols) and for $\nu = 5/3$, 8/5, 11/7, 14/9 ($\nu^* = 1, 2, 3, 4$, respectively, red symbols). The solid lines are fits to Eq. (B1). The slopes yield $m_{3/2}^* = 2.6 m_e$ for $\nu < 3/2$ and $m_{3/2}^* = 1.9 m_e$ for $\nu > 3/2$.

APPENDIX C: DATA FROM DEVICE 011

This section presents measurements from device 011. Device 011 was fabricated using the processes described in Appendix A and has top and bottom h-BN sheets with similar thickness to that of device 002. Figure 14 compares the valley isospin polarization transitions in devices 002
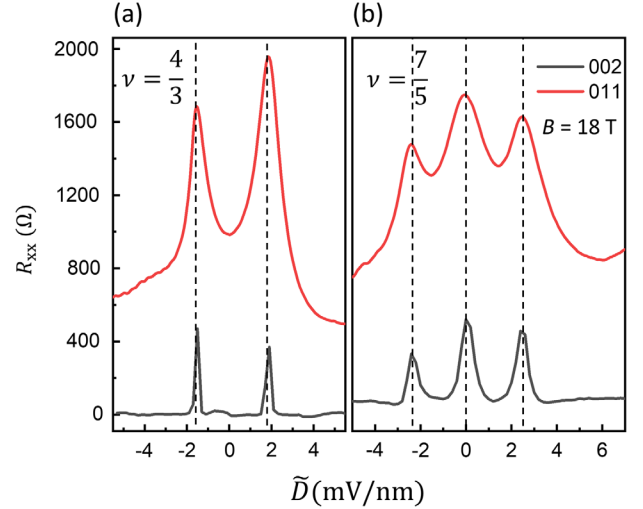

FIG. 14. Comparison of VIS polarization transitions in devices 002 (black traces) and 011 (red traces) at $\nu = 4/3$ [panel (a)] and 7/5 [panel (b)]. Here, $B = 18$ T and $T = 20$ mK. Device 011 exhibits very narrow VIS transitions shortly after the device was fabricated [see Fig. 7(d)]. Its quality degraded over many months of storage before measurements shown here were taken. Traces plotted here are three-terminal measurements, so the contact resistance is included. Nonetheless, nearly identical VIS polarization transitions are found in these two devices, indicating that the underlying physics is insensitive to sample details and relatively robust against disorder.

and 011 at two fractional states. The transitions occur at nearly identical D fields, indicating that the underlying physics is governed by the intrinsic LL structure of bilayer graphene and is insensitive to sample-specific details.

———

[1] *Perspectives in Quantum Hall Effects: Novel Quantum Liquids in Low-Dimensional Semiconductor Structures,* edited by S. Das Sarma and A. Pinczuk (Wiley, New York, 1997).

[2] *Fractional Quantum Hall Effects: New Developments*, edited by B. Halperin and J. K. Jain (World Scientific, Singapore, 2020).

[3] G. Moore and N. Read, *Nonabelions in the Fractional Quantum Hall Effect*, Nucl. Phys. **B360**, 362 (1991).

[4] N. Read and E. Rezayi, *Beyond Paired Quantum Hall States: Parafermions and Incompressible States in the First Excited Landau Level*, Phys. Rev. B **59**, 8084 (1999).

[5] C. Nayak, S. H. Simon, A. Stern, M. Freedman, and S. Das Sarma, *Non-Abelian Anyons and Topological Quantum Computation*, Rev. Mod. Phys. **80**, 1083 (2008).

[6] R. L. Willett, *The Quantum Hall Effect at 5/2 Filling Factor*, Rep. Prog. Phys. **76**, 076501 (2013).

[7] R. S. K. Mong *et al.*, *Universal Topological Quantum Computation from a Superconductor-Abelian Quantum Hall Heterostructure*, Phys. Rev. X **4**, 011036 (2014).

[8] J. Nakamura, S. Liang, G. C. Gardner, and M. J. Manfra, *Direct Observation of Anyonic Braiding Statistics*, Nat. Phys. **16**, 931 (2020).

[9] H. Bartolomei *et al.*, *Fractional Statistics in Anyon Collisions*, Science **368**, 173 (2020).

[10] R. H. Morf, *Transition from Quantum Hall to Compressible States in the Second Landau Level: New Light on the $\nu = 5/2$ Enigma*, Phys. Rev. Lett. **80**, 1505 (1998).

[11] J. I. A. Li, C. Tan, S. Chen, Y. Zeng, T. Taniguchi, K. Watanabe, J. Hone, and C. R. Dean, *Even-Denominator Fractional Quantum Hall States in Bilayer Grapheme*, Science **358**, 648 (2017).

[12] A. A. Zibrov, C. Kometter, H. Zhou, E. M. Spanton, T. Taniguchi, K. Watanabe, M. P. Zaletel, and A. F. Young, *Tunable Interacting Composite Fermion Phases in a Half-Filled Bilayer-Graphene Landau Level*, Nature (London) **549**, 360 (2017).

[13] D. K. Ki, V. I. Fal'ko, D. A. Abanin, and A. F. Morpurgo, *Observation of Even Denominator Fractional Quantum Hall Effect in Suspended Bilayer Graphene*, Nano Lett. **14**, 2135 (2014).

[14] J. Falson, D. Maryenko, B. Friess, D. Zhang, Y. Kozuka, A. Tsukazaki, J. H. Smet, and M. Kawasaki, *Even-Denominator Fractional Quantum Hall Physics in ZnO*, Nat. Phys. **11**, 347 (2015).

[15] Q. Shi, E.-M. Shih, M. V. Gustafsson, D. A. Rhodes, B. Kim, K. Watanabe, T. Taniguchi, Z. Papić, J. Hone, and C. R. Dean, *Odd- and Even-Denominator Fractional Quantum Hall States in Monolayer* WSe$_2$, Nat. Nanotechnol. **15**, 569 (2020).

[16] M. Banerjee, M. Heiblum, V. Umansky, D. E. Feldman, Y. Oreg, and A. Stern, *Observation of Half-Integer Thermal Hall Conductance*, Nature (London) **559**, 205 (2018).

[17] S.-S. Lee, S. Ryu, C. Nayak, and M. P. A. Fisher, *Particle-Hole Symmetry and the $\nu = 5/2$ Quantum Hall State*, Phys. Rev. Lett. **99**, 236807 (2007).

[18] M. Levin, B. I. Halperin, and B. Rosenow, *Particle-Hole Symmetry and the Pfaffian State*, Phys. Rev. Lett. **99**, 236806 (2007).

[19] D. T. Son, *Is the Composite Fermion a Dirac Particle?*, Phys. Rev. X **5**, 031027 (2015).

[20] K. K. W. Ma and D. E. Feldman, *The Sixteenfold Way and the Quantum Hall Effect at Half-Integer Filling Factors*, Phys. Rev. B **100**, 035302 (2019).

[21] A. Kumar, G. A. Csathy, M. J. Manfra, L. N. Pfeiffer, and K. W. West, *Nonconventional Odd-Denominator Fractional Quantum Hall States in the Second Landau Level*, Phys. Rev. Lett. **105**, 246808 (2010).

[22] B. Dutta, W. Yang, R. Melcer, H. K. Kundu, M. Heiblum, V. Umansky, Y. Oreg, A. Stern, and D. Mross, *Distinguishing between Non-Abelian Topological Orders in a Quantum Hall System*, Science **375**, 193 (2022).

[23] I. Dimov, B. I. Halperin, and C. Nayak, *Spin Order in Paired Quantum Hall States*, Phys. Rev. Lett. **100**, 126804 (2008).

[24] A. E. Feiguin, E. Rezayi, K. Yang, C. Nayak, and S. Das Sarma, *Spin Polarization of the $\nu = 5/2$ Quantum Hall State*, Phys. Rev. B **79**, 115322 (2009).

[25] J. P. Eisenstein, G. S. Boebinger, L. N. Pfeiffer, K. W. West, and S. He, *New Fractional Quantum Hall State in Double-Layer Two-Dimensional Electron Systems*, Phys. Rev. Lett. **68**, 1383 (1992).

[26] M. Padmanabhan, T. Gokmen, and M. Shayegan, *Density Dependence of Valley Polarization Energy for Composite Fermions*, Phys. Rev. B **80**, 035423 (2009).

[27] J. I. A. Li, T. Taniguchi, K. Watanabe, J. Hone, and C. R. Dean, *Excitonic Superfluid Phase in Double Bilayer Grapheme*, Nat. Phys. **13**, 751 (2017).

[28] J. Li, R.-X. Zhang, Z. Yin, J. Zhang, K. Watanabe, T. Taniguchi, C. Liu, and J. Zhu, *A Valley Valve and Electron Beam Splitter*, Science **362**, 1149 (2018).

[29] B. M. Hunt *et al.*, *Direct Measurement of Discrete Valley and Orbital Quantum Numbers in Bilayer Grapheme*, Nat. Commun. **8**, 948 (2017).

[30] J. Li, Y. Tupikov, K. Watanabe, T. Taniguchi, and J. Zhu, *Effective Landau Level Diagram of Bilayer Graphene*, Phys. Rev. Lett. **120**, 047701 (2018).

[31] J. Li, H. Fu, Z. Yin, K. Watanabe, T. Taniguchi, and J. Zhu, *Metallic Phase and Temperature Dependence of the $\nu = 0$ Quantum Hall State in Bilayer Graphene*, Phys. Rev. Lett. **122**, 097701 (2019).

[32] L. Wang *et al.*, *One-Dimensional Electrical Contact to a Two-Dimensional Material*, Science **342**, 614 (2013).

[33] J. P. Eisenstein, R. Willett, H. L. Stormer, D. C. Tsui, A. C. Gossard, and J. H. English, *Collapse of the Even-Denominator Fractional Quantum Hall Effect in Tilted Fields*, Phys. Rev. Lett. **61**, 997 (1988).

[34] L. Tiemann, G. Gamez, N. Kumada, and K. Muraki, *Unraveling the Spin Polarization of the $\nu = 5/2$ Fractional Quantum Hall State*, Science **335**, 828 (2012).

[35] G. T. Liu, C. Zhang, D. C. Tsui, I. Knez, A. Levine, R. R. Du, L. N. Pfeiffer, and K. W. West, *Enhancement of the $\nu = 5/2$ Fractional Quantum Hall State in a Small In-Plane Magnetic Field*, Phys. Rev. Lett. **108**, 196805 (2012).

[36] W. Pan, A. Serafin, J. S. Xia, L. Yin, N. S. Sullivan, K. W. Baldwin, K. W. West, L. N. Pfeiffer, and D. C. Tsui, *Competing Quantum Hall Phases in the Second Landau Level in the Low-Density Limit*, Phys. Rev. B **89**, 241302(R) (2014).

[37] N. Samkharadze, D. Ro, L. N. Pfeiffer, K. W. West, and G. A. Csáthy, *Observation of an Anomalous Density-Dependent Energy Gap of the $\nu = 5/2$ Fractional Quantum Hall State in the Low-Density Regime*, Phys. Rev. B **96**, 085105 (2017).

[38] H. M. Yoo, K. W. Baldwin, K. West, L. Pfeiffer, and R. C. Ashoori, *Complete Spin Phase Diagram of the Fractional Quantum Hall Liquid*, Nat. Phys. **16**, 1022 (2020).

[39] P. Wang, J. Sun, H. Fu, Y. Wu, H. Chen, L. N. Pfeiffer, K. W. West, X. C. Xie, and X. Lin, *Finite-Thickness Effect and Spin Polarization of the Even-Denominator Fractional Quantum Hall States*, Phys. Rev. Research **2**, 022056(R) (2020).

[40] C. R. Dean *et al.*, *Contrasting Behavior of the 5/2 and 7/3 Fractional Quantum Hall Effect in a Tilted Field*, Phys. Rev. Lett. **101**, 186806 (2008).

[41] M. P. Zaletel, R. S. K. Mong, F. Pollmann, and E. H. Rezayi, *Infinite Density Matrix Renormalization Group for Multicomponent Quantum Hall Systems*, Phys. Rev. B **91**, 045115 (2015).

[42] K. Pakrouski, M. R. Peterson, T. Jolicoeur, V. W. Scarola, C. Nayak, and M. Troyer, *Phase Diagram of the $\nu = 5/2$ Fractional Quantum Hall Effect: Effects of Landau-Level Mixing and Nonzero Width*, Phys. Rev. X **5**, 021004 (2015).

[43] E. H. Rezayi, *Landau Level Mixing and the Ground State of the $\nu = 5/2$ Quantum Hall Effect*, Phys. Rev. Lett. **119**, 026801 (2017).

[44] P. T. Zucker and D. E. Feldman, *Stabilization of the Particle-Hole Pfaffian Order by Landau-Level Mixing and Impurities That Break Particle-Hole Symmetry*, Phys. Rev. Lett. **117**, 096802 (2016).

[45] W. Zhu and D. N. Sheng, *Disorder-Driven Transition in the $\nu = 5/2$ Fractional Quantum Hall Effect*, Phys. Rev. Lett. **123**, 056804 (2019).

[46] M. Levin and B. I. Halperin, *Collective States of Non-Abelian Quasiparticles in a Magnetic Field*, Phys. Rev. B **79**, 205301 (2009).

[47] W. N. Faugno, J. K. Jain, and A. C. Balram, *Non-Abelian Fractional Quantum Hall State at 3/7-Filled Landau Level*, Phys. Rev. Research **2**, 033223 (2020).

[48] R. R. Du, A. S. Yeh, H. L. Stormer, D. C. Tsui, L. N. Pfeiffer, and K. W. West, *Fractional Quantum Hall Effect around $\nu = 3/2$: Composite Fermions with a Spin*, Phys. Rev. Lett. **75**, 3926 (1995).

[49] B. E. Feldman, A. J. Levin, B. Krauss, D. A. Abanin, B. I. Halperin, J. H. Smet, and A. Yacoby, *Fractional Quantum Hall Phase Transitions and Four-Flux States in Graphene*, Phys. Rev. Lett. **111**, 076802 (2013).

[50] A. C. Balram, C. Tőke, A. Wójs, and J. K. Jain, *Fractional Quantum Hall Effect in Graphene: Quantitative Comparison between Theory and Experiment*, Phys. Rev. B **92**, 075410 (2015).

[51] Z. Papić and D. A. Abanin, *Topological Phases in the Zeroth Landau Level of Bilayer Graphene*, Phys. Rev. Lett. **112**, 046602 (2014).

[52] D. Rhodes, S. H. Chae, R. Ribeiro-Palau, and J. Hone, *Disorder in van der Waals Heterostructures of 2D Materials*, Nat. Mater. **18**, 541 (2019).

[53] E. McCann and M. Koshino, *The Electronic Properties of Bilayer Grapheme*, Rep. Prog. Phys. **76**, 056503 (2013).